Phase retrieval using plasmonic nanostructures

Master thesis

Carolina Rendón Barraza

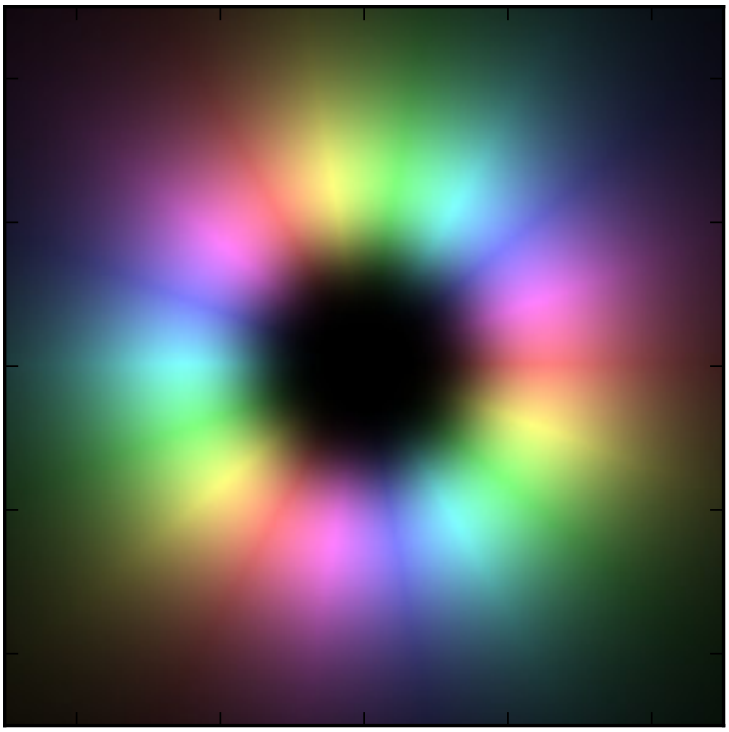

Supervisors

Prof. Dr. Eric R. Eliel
Ir. Philip F. Chimento

Leiden University, Quantum Optics Group, January 2012

Contents

Chapter 1

Introduction

In optics, retrieving the phase information of light is a classic problem that cannot be solved by direct measurement since measurement devices only record the intensity of light, not the amplitude and phase. Indirect measurement to obtain the phase of light is usually made by means of interference that produces a fringe pattern from which the phase can be extracted.

In this research, we will examine a different method. We employ surface plasmon excitations to locally probe the electromagnetic field of an incoming optical vortex beam. We choose to analyze optical vortex beams as they have a well-defined phase structure, although the principle of this method should allow to analyze an arbitrary (unknown) input beam.

Surface plasmons (SPs) are travelling oscillations of the electron plasma in a metal. They are bound to the surface of a metal and can be generated by light radiation incident on a corrugation of the metal surface. We will use a microscopic slit in a gold film as a localized coupler to the incident light. At a distance there is another, but larger, slit receiving the generated surface plasmons from the first slit in order to convert them back into photons which can then in turn be imaged by a camera.

By scanning the incident beam we construct a tomogram. A tomogram is the result of plotting three-dimensional data into two-dimensional sections without loss of information. SPs are a convenient tool for this tomography, because they propagate in two dimensions and because we can achieve subwavelength resolution in our tomograms by translating the subwavelength slits in subwavelength steps. Since the light-plasmon coupler maintains the phase, the tomogram will be sensitive to phase differences along the scanned trajectory.

In Chapter 2 we will provide a brief description of the phase retrieval problem together with some classical methods and their limitations. We also provide a small theoretical description of surface plasmons. Furthermore, we give an abstract of the Huygens–Fresnel principle which describes a model of how SPs are generated and travel across the metal-dielectric interface. And finally, we describe a surface defect scattering, where we learn about the way in which SPs are generated and converted into free space light.

In Chapter 3 we provide a brief description of our proposed method to solve the phase retrieval problem. We describe the construction of computational simulations and we discuss their results, which provide an expectation for the physical experiment.

In Chapter 4 the experiment is described as performed in the lab. We describe the three main experimental setups that we constructed as well as the components used in them. Finally, the results attained from this experimental work are presented.

And finally, in Chapter 5, we present the conclusions of this project together with some recommendations for future projects.

Chapter 2

General Theory

2.1 Previous work

2.1.1 Phase retrieval

Measurements of a complex-valued signal are required in many scientific and technological areas, such as astronomy [1] and X-ray crystallography [2]. Unfortunately, they must be made with sensors that can only observe the signal's intensity while in general, important features of a signal are preserved in phases. For the reconstruction of both one-dimensional and multi-dimensional signals, the magnitudes and the phases of the Fourier transform play different roles.

Phase retrieval is the process of recovering the phase, given just the magnitude, of a signal's Fourier transform, thereby recovering the signal itself. Phase retrieval determines the phase error or aberrations of an optical system. Knowledge of the aberrated wave front can subsequently be used to design correction optics for the system in order to obtain imagery of higher quality. There is not a straightforward method of performing phase retrieval. However, the first widely accepted phase retrieval algorithms, mainly for nonperiodic objects, were developed in 1971 by Gerchberg and Saxton [3], and in 1978 by Fienup [4]. In general, their idea was that if partial information about the magnitude of the input signal as well as about the magnitude of the signal's Fourier transform can be supplied, the phase information may be recovered. Phase retrieval algorithms [5] use computer modeling that is run several times, giving a pattern as a result. It is from the comparison of this pattern to the known data of the actual optical system that the correct parameters can usually be determined and used to accurately model the system.

Phase retrieval algorithms, as the different existing methods so far, require *a priori* signal assumptions to solve phase retrieval problems with complex signals. In many physical scenarios, the phase retrieval process can be time consuming or expensive.

2.1.2 Wavefront sensing

Wavefront sensing, usually applying phase retrieval algorithms, can provide the means to measure the shape of an optical wavefront. Since the birth of modern adaptive optics in 1953 [6] wavefront sensors have played an important role in the design of adaptive optics systems.

Adaptive optics is a technology used to improve the performance of optical systems by reducing the effect of wavefront distortions. It is used in astronomical telescopes and laser communication systems to remove the effects of atmospheric distortion, and in retinal imaging systems to reduce the impact of optical aberrations.

Wavefront sensors may be used either to generate a signal related to the wavefront deformation, or to provide a full reconstruction of the wavefront shape. The phase of a wavefront can be measured directly or indirectly in a number of ways [7]. Direct methods include interferometric methods, Fraunhoffer diffraction patterns, moments of diffraction and multiple intensity measurements. It can also be measured indirectly, by compensating for the wavefront error without explicitly calculating the full wavefront reconstruction (multi-dither technique).

One example is the Shack-Hartmann wavefront sensor, which provides a measurement of the local first derivative (slope) of the input wavefront. Although it has some advantages that make it the most widely used sensor, it also has some drawbacks, such as the precision required in alignment and calibration of this device. Vibration or distortion of the optics could lead to shifts in the spot positions, which in turn would give incorrect measurements of the wavefront slope. A second disadvantage is that this type of wavefront sensor is not well suited to dealing with extended sources. Finally, the number of pixels required in the detector to create one phase data point is much higher than in other sensors. For high spatial resolutions large CCD cameras are required and this can be expensive and adds extra weight to the optical system.

Another example is the curvature sensor, a special class of wavefront sensor which measures the local wavefront curvature using a pair of intensity images with equal and opposite aberration, captured symmetrically about the image plane of the optical system. The wavefront phase can be calculated from the relative intensities using iterative algorithms. These solutions are computationally expensive and the time taken to calculate the solution sometimes is not sufficiently short for real-time adaptive optics applications.

Some other examples, such as the hybrid wavefront sensor which combines the Shack-Hartmann and curvature sensors, are discussed in reference [7] together with a short description of their own advantages and disadvantages. In general, the author shows that direct measurement of the wavefront phase can be computationally very expensive, but in indirect methods the burden is shifted to the accurate measurement of the chosen quality metric. At the end, the selection of a method mainly depends on the application.

In this work, we aim for finding an alternative method for determining the phase of an input wavefront to the ones referred above. Our inspiration comes from [8], and it makes use of the properties of surface plasmons described in section 2.2. As in the reference, the experiment employs a subwavelength slit in a gold film to cut slices from a beam with a certain phase distribution in the transverse plane and measure the diffraction of the surface plasmons by scattering them off a second "infinite"[1] slit. The main difference in the work presented here with that in [8], is that by moving the slits across the vortex beam, we try to determine the phase of the incident beam.

[1] For practical purposes

2.2 Physical Phenomena

2.2.1 What is a surface plasmon?

A surface plasmon is an electromagnetic oscillation on the surface of a metal due to its free electrons which can easily interact with incident light, becoming involved in a series of optical phenomena, such as enhanced photoeffect by SPs or surface enhanced Raman scattering. This interaction occurs mainly in corrugated surfaces that act as couplers and this coupling can be in both directions, with SPs radiating light and with light exciting SPs. Simple isolated surface defects such as a groove or a slit on an otherwise planar surface can also provide a mechanism for exciting SPs.

The physics of SPs follows traditionally from Maxwell's equations describing the electromagnetic field caused by the free electrons on an interface between a metal and a dielectric. These electrons are considered as an electron liquid whose density fluctuates longitudinally and propagates through the bulk plasmons of the metal. Surface plasma oscillations, as they are alternatively named, have a frequency ω tied to their wave vector k_{sp} by a dispersion relation $\omega(k_{sp})$, and are accompanied by an electromagnetic field which disappears at $|z| \to \infty$ as it decays exponentially away from the maximum at the surface ($z = 0$) and can be written as (Fig. 2.1)

$$E = E_0^{\pm} \exp\left[i(k_{sp}x \pm k_z z - \omega t)\right] \tag{2.1}$$

using $+$ for $z \geq 0$ and $-$ for $z \leq 0$. Here $k_{sp} = 2\pi/\lambda_{sp}$ where λ_{sp} is the wavelength of the plasma oscillation and k_z is imaginary, which causes the decay of the field E_z. Note that $k_{z>0} \neq k_{z<0}$ as k_z depends on the dielectric constant of either the diectric layer or the metal.

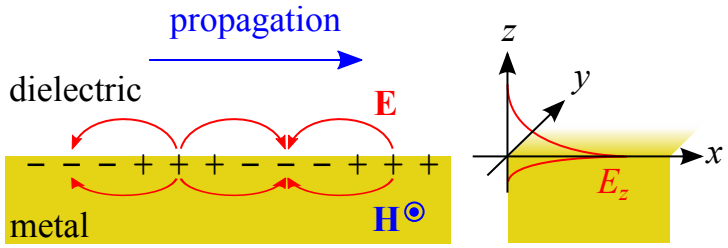

Figure 2.1: Schematic picture of the charge distribution of a surface plasmon and the associated electromagnetic wave.

The Maxwell's equations for this specific geometry (metal plane surface - dielectric interface) together with Eq. 2.1 result in the dispersion relation [9, pp. 4-7]

$$k_{sp}^2 = \frac{\omega^2}{c^2}\frac{\epsilon_d \epsilon_m(\omega)}{\epsilon_d + \epsilon_m(\omega)}, \tag{2.2}$$

where ϵ_d is the dielectric constant of the dielectric material, $\epsilon_m(\omega)$ is the frequency-dependent dielectric function of the metal, and c is the speed of light. The electric field of the surface

plasmon has both longitudinal (x) and transverse (z) components. Surface plasmons can be most elegantly described by the associated magnetic field H_y as it is purely transverse.

Surface plasmons are attenuated during propagation, basically due to dissipation in the metal or re-radiation as light if the surface is not smooth or in the Kretschmann configuration[2]. The field attenuation length, L_{sp}, is

$$L_{sp} = \frac{1}{2k''_{sp}} \tag{2.3}$$

where k''_{sp} is the imaginary part of the propagation constant of a SP (in Eq. 2.2, ϵ_m has a complex value). L_{sp} is the length after which the intensity decreases by $1/e$ and for gold and silver extends from millimeters in the mid-infrared range to less than a micron in the blue part of the visible spectrum. The surface roughness causes the SP energy to couple to light, i.e. it radiates into the environment.

2.2.2 Huygens-Fresnel principle for surface plasmons

The Huygens - Fresnel principle is a method of analysis applied to problems of wave propagation both in the far-field limit and in near-field diffraction. Dutch physicist Christiaan Huygens considered every point of a given wavefront of light as a source of secondary spherical wavelets and French physicist Augustin-Jean Fresnel added the assumption that the actual field at any point beyond the wave front is a superposition of all of them.

Surface plasmons behave differently from light in a number of ways, such as propagation, interference and diffraction, and are bound to a two-dimensional surface. Therefore, an adapted form of the general (three-dimensional) Huygens-Fresnel principle for surface plasmons should be considered.

A general representation of a surface plasmon field along a planar surface $z = 0$ in the direction of positive x (i.e. the propagation direction of the SP) is given by [10, 11]:

$$H_y^{sp}(x,y) = \int \frac{dk_y}{2\pi} H_y^{sp}(k_y) e^{i\sqrt{k_{sp}^2 - k_y^2}x + ik_y y} \tag{2.4}$$

Eq. 2.4 represents a cylindrical wave, hence, we can make use of the Hankel function[3] in the asymptotic form, valid for distances larger than the wavelength. This results in:

$$H_y^{sp}(x,y) = -\frac{i}{\sqrt{\lambda_{sp}}} e^{i\pi/4} \int dy' \cos\theta H_y^{sp}(x=0,y') \frac{e^{ik_{sp}\rho}}{\sqrt{\rho}} \tag{2.5}$$

where $\lambda_{sp} = 2\pi/k_{sp}$ is the surface plasmon wavelength, $\rho = \sqrt{x^2 + (y-y')^2}$ and $\theta = \arccos(x/\rho)$. Here, the propagator is a damped cylindrical wave $e^{ik_{sp}\rho}/\sqrt{\rho}$ instead of the spherical wave e^{ikr}/r in the case of light propagation in a 3D vacuum. The derivation of Eq. 2.5 is given in [11].

[2] In the Kretschmann configuration, the light illuminates the wall of a glass block, typically a prism, and is totally internally reflected. A thin metal film (for example gold) is evaporated onto the glass block. The light again illuminates the glass block, and an evanescent wave penetrates through the metal film. SPs are excited at the outer side of the film.

[3] The Hankel functions are used to express propagating cylindrical wave solutions of a cylindrical wave equation.

Eq. 2.5 can be viewed as a Huygens-Fresnel principle for surface plasmons, in which the surface plasmon field at (x, y) is resulting from the interferences of surface plasmons emitted by secondary sources located at $(x = 0, y')$ with an amplitude $E_z^{sp}(x = 0, y')$. Also, the phase of the surface plasmon field can be calculated from its complex amplitude.

The integral in Eq. 2.5 is the Fourier transform of the product of two functions of k_y and by employing the convolution theorem,[4] we can rewrite it as a convolution product in direct space:

$$H_y^{sp}(x, y) = \int dy' \; H_y^{sp}(x = 0, y') \cdot h(x, y - y') = H_y^{sp}(0, y) * h(x, y) \tag{2.6}$$

where $h(x, y)$ is the convolution kernel and can be rewritten as:

$$h(x, y) = \frac{-i}{\sqrt{\lambda_{sp}}} e^{i\pi/4} \frac{x}{\rho} \frac{e^{ik_{sp}\rho}}{\sqrt{\rho}} \tag{2.7}$$

Eq. 2.6 is used in the numerical calculation of the two-slit system in the experiments described in this text.

2.2.3 Surface-plasmon excitation

When not in Kretschmann configuration, because a SP is a bounded mode, i.e. it decays exponentially on both the metal and the dielectric sides, it cannot be directly excited when a flat interface is illuminated by a plane wave, even at highly oblique incidence. However, SPs are launched whenever there exists a perturbation in the smooth surface, for example, by etching a subwavelength indentation in a metal thin film.

The value of the SP wave number k_{sp} is larger than that of the light in free space k_0. Consequently, there is a wave vector mismatch between the surface plasmon and free space radiation, and it is therefore not possible to directly excite the SP by light on a smooth bulk metal surface. By adding a defect on the surface, the diffraction order in the incident beam changes and the wave vector $k = \omega/c$ is increased by a Δk_x value allowing the photons to be transformed into SPs.

The polarization of the incident radiation has also to be chosen so as optimally couple with a surface plasmon. In our experiments, we use two slits to launch and detect surface plasmons and the incident light is polarized perpendicular to the slit axis.

The present work focuses on a two-slit system. Each slit functions as a coupler, thus scattering part of incident light into a plasmonic channel, and as a decoupler, turning a surface plasmon back into free space radiation. The separation between the slits is comparable to the decay length of the surface plasmons (Ch. 3) to allow a generated SP to reach the other slit. The direct transmission at the two slits would also give rise to conventional Young-type interference

[4]The convolution theorem states that

$$F\{f \cdot g\} = F\{f\} * F\{g\}$$

where $F\{f\}$ denotes the Fourier transform of f and * denotes the convolution operation.

patterns as described in [12]. In our experiment however, we tried to prevent illumination of one of the slits in order to avoid this interference.

When the incident light is TM-polarized the surface plasmon that is excited at one of the slits propagates towards its partner slit where it is partially converted into light again. If not avoided, the plasmon amplitude would interfere with the amplitude of the light that is directly transmitted by the same slit. The plasmon amplitude is weaker than the direct transmission at the first slit because the plasmon has lost amplitude due to reconversion into light, reflection and/or transmission (through the indentation) [13]. This would unfavorably make the direct transmission light intensity overcome the plasmon intensity.

2.2.4 Surface defect scattering

As mentioned in [13], recent experimental studies on SP scattering by single surface defects have shown evidence of drastically distinct scattering properties depending on the defect size. In search of a theoretical explanation that is still missing, the authors focus on the case of one-dimensional surface defects, including near-field and far-field calculations and their dependence on defect size parameters. Specially, they analyze the SP-photon coupling, looking for the adequate defect parameters that maximize radiation.

The work showed that in the case of wide indentations, the behavior differs from that for protuberances, and exhibits a richer phenomenology. Upon increasing the width of the indentation, transmission of the SP, along the surface and through the defect, reaches a minimum value leading to maximum radiation, and then slowly grows towards total transmission (no radiation) in an oscillatory manner. Defect depth determines the oscillations and the value of the defect width that results in a maximum radiation. The increase of the SP transmission starts from an absolute minimum in transmission for small half-widths. The period of the oscillations is related to the defect impedance, that is in a way reminiscent of a cavity-like effect. It is reported that for sufficiently deep indentations, this maximum radiation value can be extremely large (even larger than 90%), so that the Gaussian indentation thus behaves as a light emitter.

In our experiment we chose to have slits (indentations) that strongly couple radiation and SPs in order to be able to observe the re-emitted light. The indentation must be sufficiently deep ($d/\lambda_{sp} > 0.2$). According to [13], the ideal width of the slits for maximum coupling cannot be exactly determined so far. We chose slits of 100 nm wide and 200 nm deep. It satisfied the depth requirement for the wavelength ($\approx$ 800 nm) and this width proved effective in earlier experiments [16].

Chapter 3

Numerical simulations

In a general way, the experiment consists of the generation of SPs by scattering an incoming vortex beam off a narrow emitter slit milled in a gold film (Fig. 3.1). The incident beam is TM-polarized in order to allow coupling to SPs [12]. A second receiver slit picks up the diffracted SP wave, converting it back to free-space optical radiation. We translate the sample along the positive x-axis and y-axis in 0.1 μm and 1 μm increments so that the emitter slit travels through the incident beam and the gold film translates transversely to the optical axis of the vortex beam. We image the light emerging from the receiver slit on a CCD and record this illumination pattern. We stitch the various recorded patterns together and this way, we construct a tomographic pattern of the plasmonic diffraction where each vertical slice of the tomogram corresponds to one slice of the incident vortex beam after propagation from emitter to receiver.

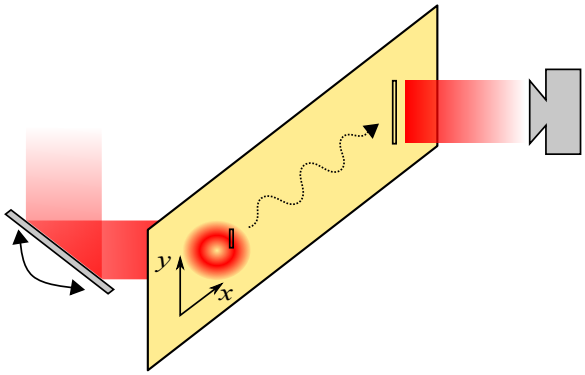

Figure 3.1: SPs are generated by scattering an incoming vortex beam off a narrow emitter slit milled in a gold film. A second receiver slit picks up the diffracted SP wave, converting it back to free-space optical radiation. We translate the sample along the positive x-axis and y-axis so that the emitter slit travels through the incident beam and the gold film translates transversely to the optical axis of the vortex beam. We image the light emerging from the receiver slit on a CCD and record this illumination pattern.

The sample consists of a gold film, 200 nm thick, attached to a glass substrate by a 10 nm titanium adhesion layer. The titanium layer ensures that SPs can only propagate from emitter to receiver slit on the gold-air interface. The sample contains pairs of double slits that are ion-beam milled through the gold. The slits used in this experiment are 2 μm (emitter) and 50 μm (receiver) long, 100 nm wide, and are separated by 75 μm. For comparison, the

damping length of SPs on gold at $\lambda = 830$ nm is around 50 μm. This value is calculated as done similarly in [9, p. 7], using Eq. 2.3 in which the complex dielectric constant of gold is given by $\epsilon_m = n_m^2/\mu$. Here $\mu \approx 1$ for this wavelength and n_m is given in Table 3.1.

An optical vortex is a beam of light whose phase varies in a corkscrew-like manner along the beam's direction of propagation. There are several types of phase singularities in a monochromatic light wave, and the necessary condition for their existence is that the wave amplitude vanishes at the singularity, resulting in a "dark spot" within a light wave, where the phase becomes undetermined. Optical vortices are topological objects on wavefront surfaces which possess so-called topological charge, or vortex charge, attributed to the structure of the wavefront around a phase singularity: a positive charge $Q > 0$ is attributed to a right-handed helicoid, and the sign of the charge is negative for a left-handed helicoid. The vortex charge Q determines the number of cycles with which the phase increases on a closed loop around the vortex. An ordinary plane (or spherical, or Gaussian) wave without any phase singularity is uncharged, $Q = 0$.

The amplitude and phase structure of a singular beam depends on the "host" beam that is used. In the most common case, the incident beam has a Gaussian amplitude profile centered at a radius $r = 0$ with the waist plane coinciding with plane $z = 0$. The expression for a Gaussian light wave carrying a Q-charged axial optical vortex written in polar coordinates is [14]

$$E(r,\theta) = E_0 \frac{\rho}{\sqrt{2}}\, e^{-iQ\theta} e^{-\rho^2/2} \left[I_{\frac{|Q|-1}{2}}\left(\rho^2/2\right) - I_{\frac{|Q|+1}{2}}\left(\rho^2/2\right) \right] \tag{3.1}$$

where $\rho = r/w_0$, w_0 is the host beam waist parameter[1] and I_α is the modified Bessel function of the first kind. The host Gaussian beam is expressed in its simplest form as an unbounded plane wave

$$E(r) = E_0 e^{-\rho^2} \tag{3.2}$$

where we chose $E_0 = 1$. Eq. 3.2 represents the amplitude distribution in the waist plane of a lowest-order transverse electromagnetic Gaussian-beam wave.

The transverse cross section of a vortex beam has a doughnut-shaped intensity distribution. The phase increases azimuthally around the doughnut and the intensity vanishes at the center because the phase is undefined there. Figure 3.2 represents the intensities of the three input beams used in the computer simulations in section 3.1. The first one (a) corresponds to a Gaussian beam in its focus ($\lambda_0 = 830 \times 10^{-9}$ m) with a waist parameter $w_0 = 15$ μm and the other two are vortex beams generated with the aforementioned Gaussian beam as a host beam through Eq. 3.1 with charges (b) $Q = 1$ and (c) $Q = 3$. Notice that for $Q = 0$, Eq. 3.1 reduces to $E(r) = E_0 \sqrt{\frac{\pi}{2}}\, e^{-\rho^2}$ which is proportional to Eq. 3.2.

Fig. 3.3 represents the phase of these beams in the transverse plane.

[1]The waist parameter of a Gaussian beam is the distance from the beam axis where the optical intensity drops to $1/e^2$ of the value on the beam axis.

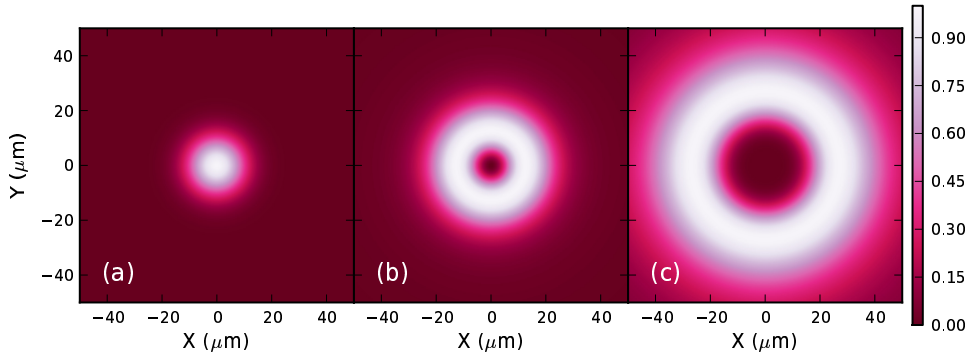

Figure 3.2: Transverse cross sections of (a) a Gaussian beam and of a vortex beam with (b) $Q = 1$ and (c) $Q = 3$. The waist parameter of the host Gaussian beam is $w_0 = 15$ μm for the three profiles.

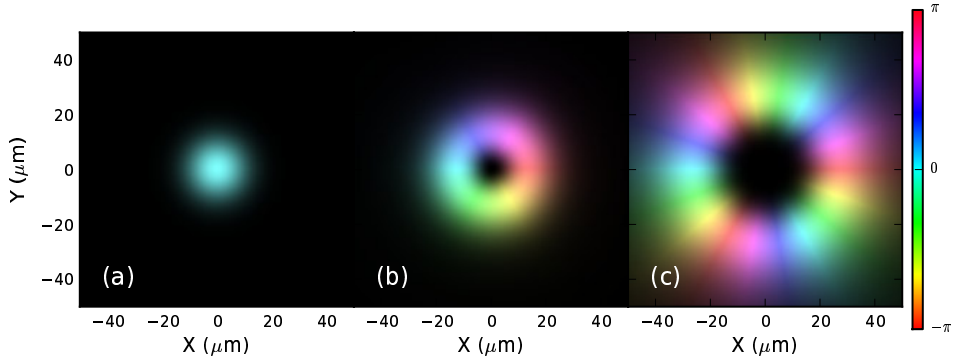

Figure 3.3: Phase distribution of (a) a Gaussian beam and of vortex beams with (b) $Q = 1$ and (c) $Q = 3$. The waist parameter of the host Gaussian beam is $w_0 = 15$ μm for the three profiles.

3.1 Tomograms creation

We calculate the expected tomograms by modeling the emitter slit as a SP source with its field amplitude proportional to the free-space field amplitude of the incident vortex beam (Eq. 3.1) at that point on the sample. We then calculate the evolution of this field under propagation from emitter to receiver, using the Huygens-Fresnel principle in the form of Eq. 2.6. We model the receiver slit as a line, which scatters SPs into free-space light whose amplitude is proportional to the SPs amplitude it receives.

Figures 3.5 to 3.11 show the calculated tomograms for incident vortex beams. The vortex beams have a charge $Q = 1, -1, 3$ or -3. Tomograms of incident Gaussian beams are expected to be similar to those with incident $Q = 0$ vortex beams, therefore they won't be displayed separately. The values listed in Table 3.1 are the ones inserted into the simulations and correspond to the real physical values used in the experiment. There are two possible ways to translate the input beam along the SP emitter slit, horizontally (x-direction) and vertically (y-direction). Horizontal movement is in all cases, performed through the center of the beam. For vertical movements, we define d_0 as the distance from the center point of the respective incoming beam to the position of the path in which the emitter receiver is translated (Fig. 3.4).

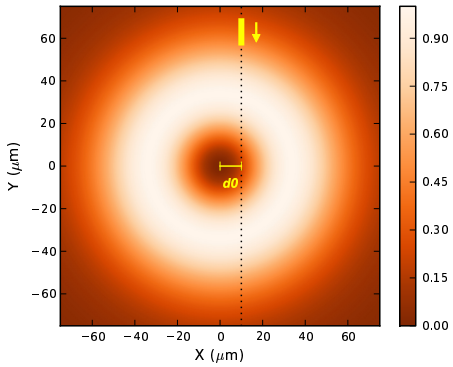

Figure 3.4: Example of a vortex beam $Q = 1$ with host beam's waist parameter $w_0 = 40$ μm where the emitter slit travels along the dotted line at a distance $d_0 = 10$ μm from the center. In this example, the emitter slit is 10 μm long for clarity purposes.

$l = 2 \times 10^{-6}$ m	SP emitter slit length.
$L = 50 \times 10^{-6}$ m	SP receiver slit length and size of simulation domain.
$res = 1 \times 10^{-7}$ m	Size of a pixel.
$\lambda_0 = 830 \times 10^{-9}$ m	Light wavelength in free space.
$n_{Au} = 0.18927 + (5.4182)i$	Index of refraction of gold at 830 nm [15, pp. 286-295].
$\epsilon_d = 1$	Dielectric constant of dielectric (air), $n = 1$.
$w_0 = 7 \times 10^{-6}$ m	Waist parameter of Gaussian beam.

Table 3.1: Physical values used for tomogram calculation reported in this section.

In the following simulations (Figs. 3.5 to 3.11) it is not considered that direct light could travel through the SP receiver, i.e. only the light proceeding from SP transmission is taken into account.

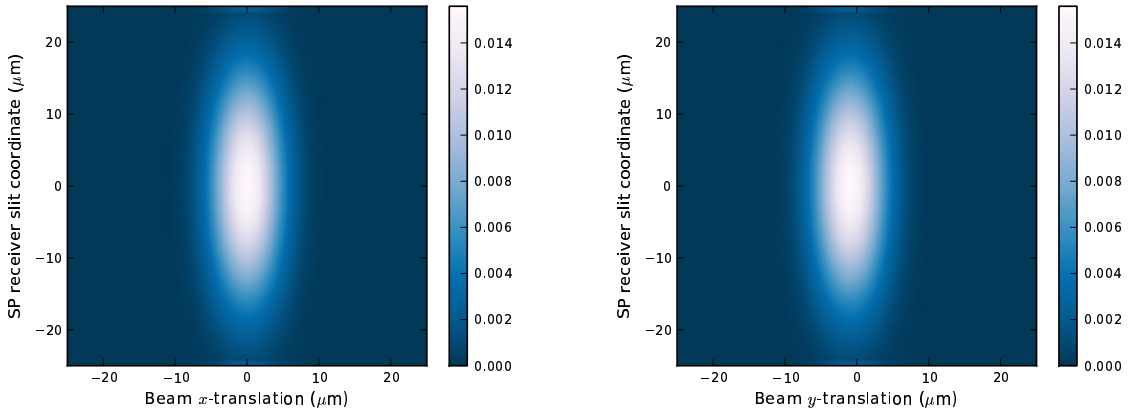

(a) (b)

Figure 3.5: Tomograms corresponding to a Gaussian beam in (a) horizontal movement through the beam's center and in (b) vertical movement through the beam's center ($d_0 = 0$). The elongated shape of the spots visualized in the tomograms are due to the length of the receiver slit. They are almost alike because the input beam is rotationally invariant about the optical axis and because the size of the emitter slit is small compared to the size of the beam. Therefore, the light arriving to the emitter slit at each step during the vertical movement has the same phase and the intensity varies almost in the same way than in the horizontal movement.

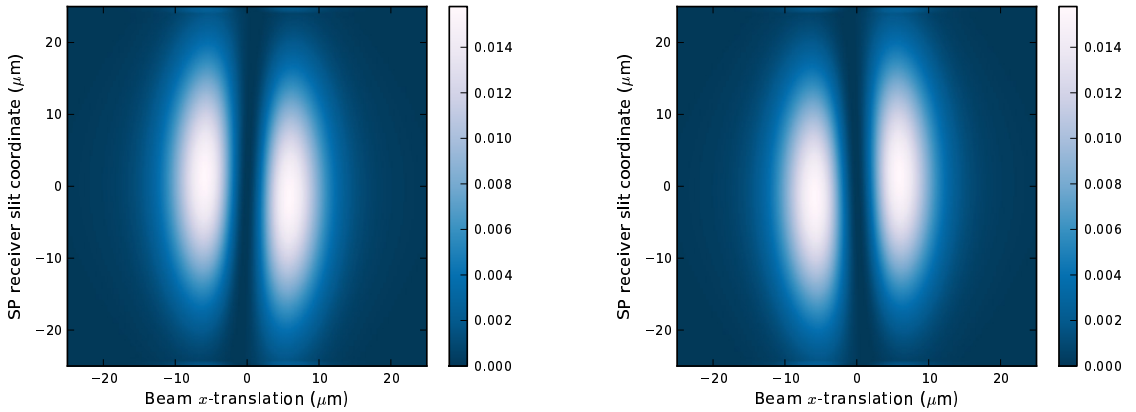

(a) (b)

Figure 3.6: Tomograms of a vortex beam in horizontal movement through the beam center, (a) $Q = 1$ and (b) $Q = -1$. They are each other's mirror because their phase profiles are mirrored.

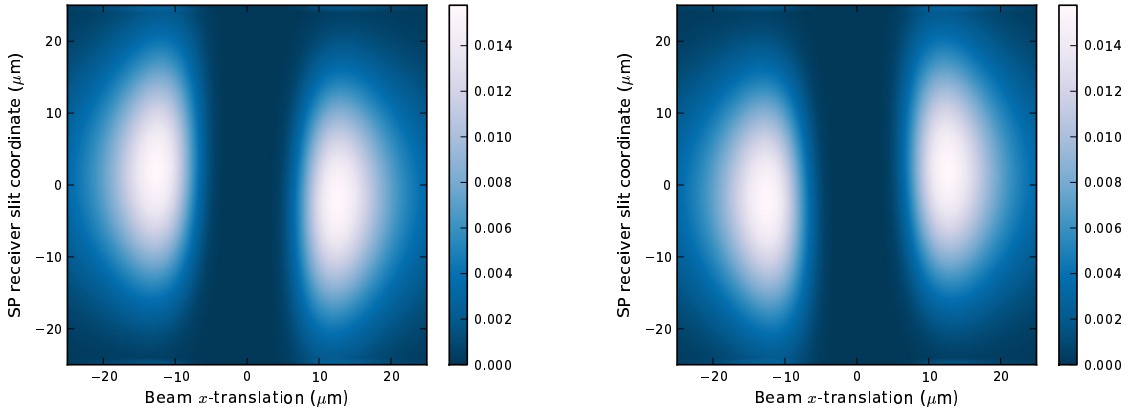

(a) (b)

Figure 3.7: Tomograms of a vortex beam in horizontal movement through the beam center, (a) $Q = 3$ and (b) $Q = -3$. They are each other's mirror because their phase profiles are mirrored.

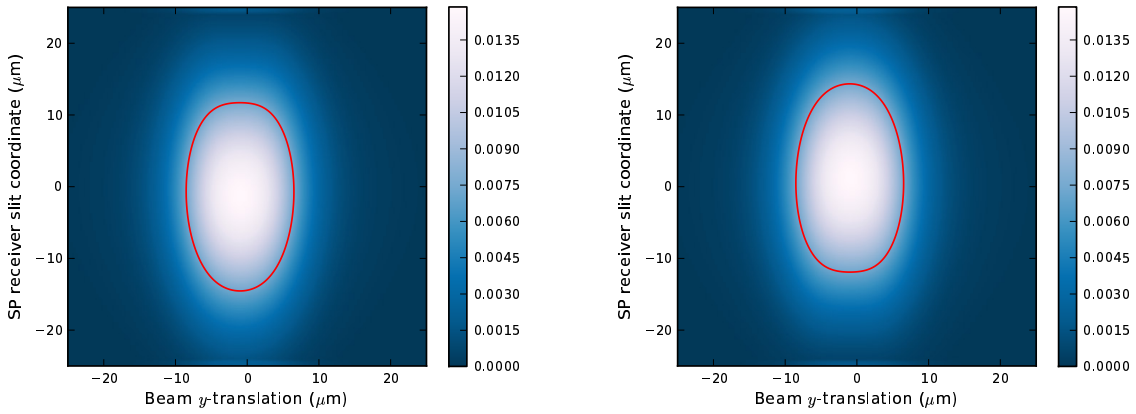

(a) (b)

Figure 3.8: Tomograms of a vortex beam in vertical movement outside the beam center ($d_0 = 7$ μm), (a) $Q = 1$ and (b) $Q = -1$, presenting ovoid shapes with opposite orientation (highlighted in red).

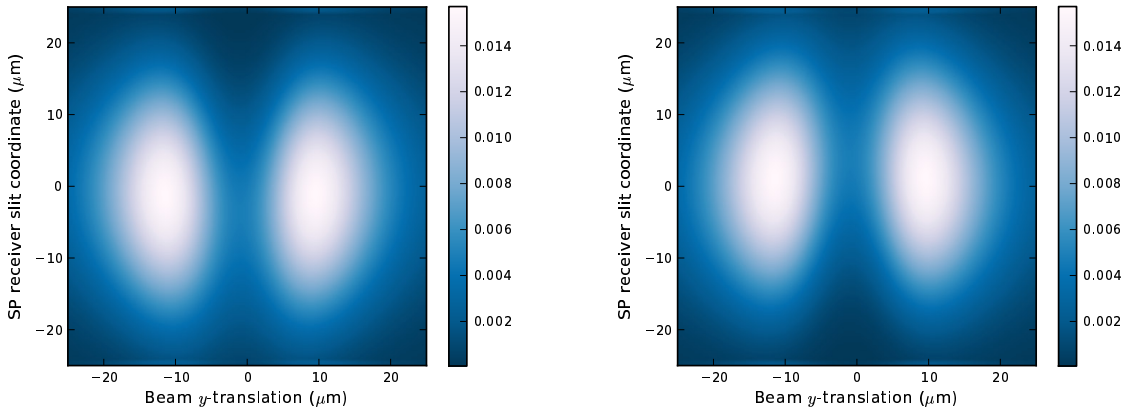

(a) (b)

Figure 3.9: Tomograms corresponding to a vortex beam in off-center vertical movement with $d_0 = 7$ μm, (a) $Q = 3$ and (b) $Q = -3$.

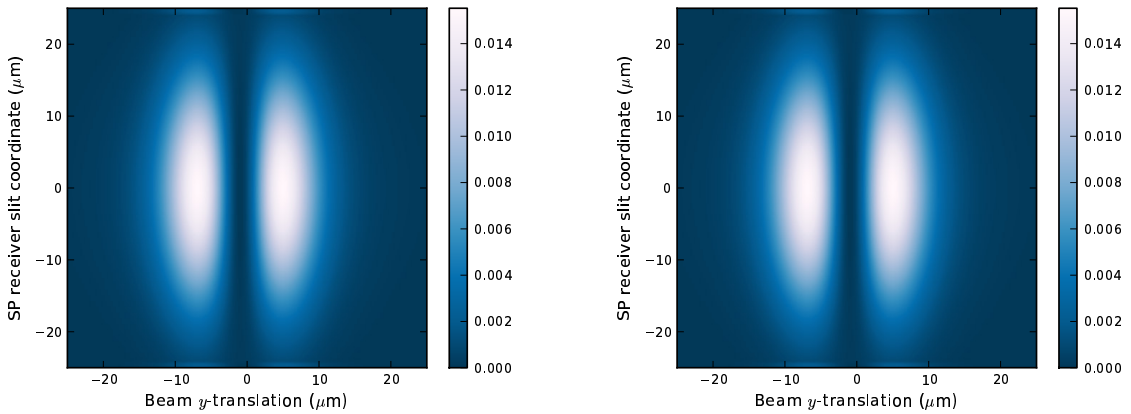

(a) (b)

Figure 3.10: Vertical scan of a vortex beam through the center ($d_0 = 0$), (a) $Q = 1$ and (b) $Q = -1$. Compared with Fig. 3.6, these aren't slanted because the slit only travels through two constant phases.

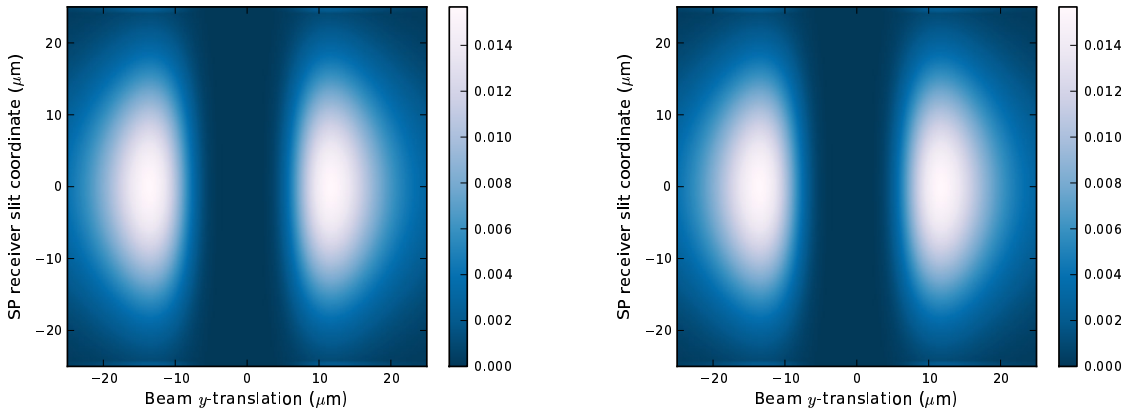

(a) (b)

Figure 3.11: Vertical scan of a vortex beam through the center ($d_0 = 0$), (a) $Q = 3$ and (b) $Q = -3$. Compared with Fig. 3.7, these aren't slanted because the slit only travels through two constant phases.

Because the experiments suggest that this may be happening, for the next set of figures (Figs. 3.12 to 3.14) we considered that some remaining direct light can travel through the SP receiver slit and therefore, interfere with scattered SPs. We model this simply by calculating the field generated by the scattered SPs plus the field of the transmitted light of the vortex beam through the receiver slit. The field transmission coefficient that we used, $T = \sqrt{0.38}$, was determined experimentally in [16]. We calculated waist parameters matching the ones used in our experiments (Ch. 4) and we only show vertical movement calculations because most of the experimental results were obtained in that direction.

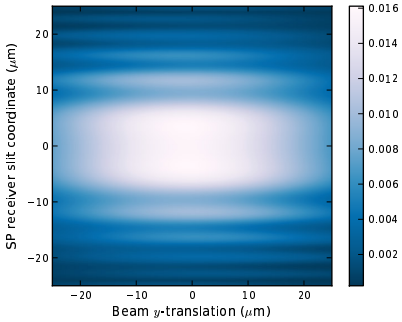

Figure 3.12: Tomogram corresponding to a Gaussian beam with waist parameter $w_0 = 40$ μm in vertical movement with $d_0 = 7$ μm. Without the interference added we should obtain a tomogram similar to the one showed in Fig. 3.5(b).

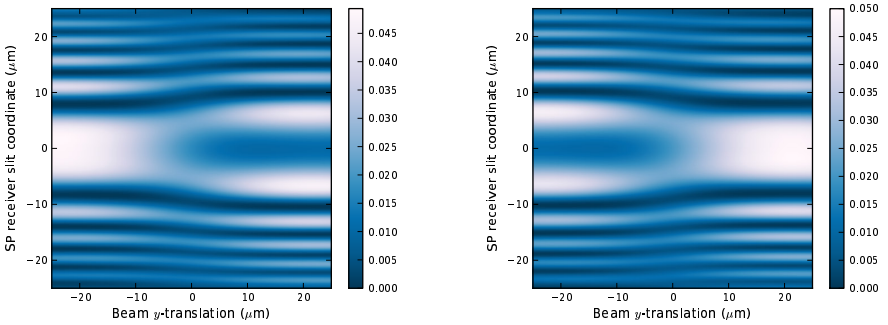

(a) (b)

Figure 3.13: Tomograms corresponding to a vortex beam in vertical movement with $d_0 = 7$ μm. (a) $Q = 1$ and (b) $Q = -1$. The waist parameter of the host Gaussian beam is $w_0 = 30$ μm. Compare to Fig. 3.8 for no interference tomograms.

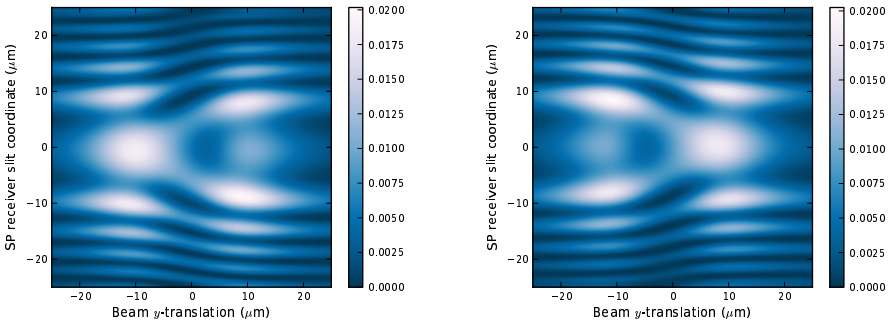

(a) (b)

Figure 3.14: Tomograms corresponding to a vortex beam in vertical movement with $d_0 = 7$ μm. (a) $Q = 3$ and (b) $Q = -3$. The waist parameter of the host Gaussian beam is $w_0 = 7$ μm. Compare to Fig. 3.9 for no interference tomograms.

In order to provide a better visualization of how the simulations are constructed, we show with two examples (Figs. 3.9 and 3.14) the profile intensities in three different positions of the tomograms (Figs. 3.15 and 3.16).

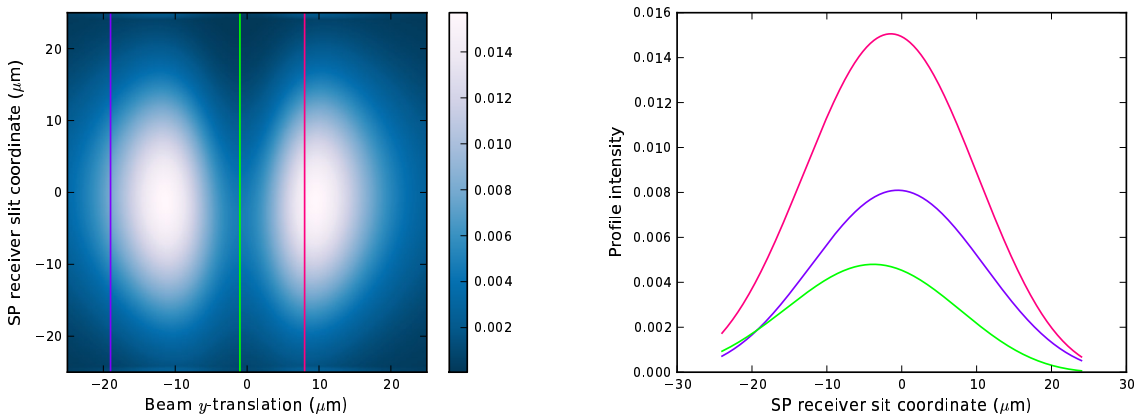

(a) (b)

Figure 3.15: Intensity profiles on the receiver slit for selected positions of the vortex beam in Fig. 3.9(a).

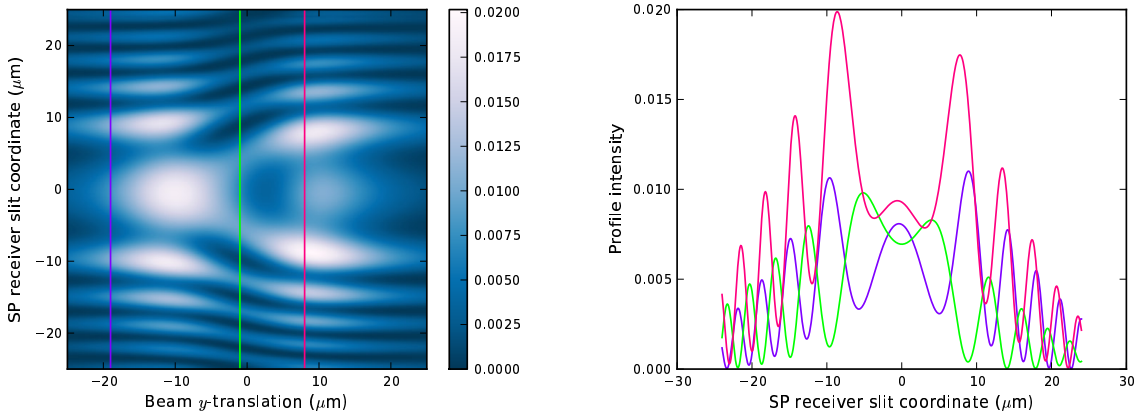

(a) (b)

Figure 3.16: Intensity profiles on the receiver slit for selected positions of the vortex beam in Fig. 3.14(a).

3.2 Discussion

Figure 3.5 shows the results for two tomograms of a Gaussian beam, one in horizontal movement through the beam's center and the other in vertical movement through the beam's center ($d_0 = 0$). Note that both translations are almost indistinguishable. This happens because the input beam is rotationally invariant about the optical axis. Therefore, in both movements, the light arriving to the emitter slit has the same phase and the intensity varies in the same way. The angle of the emitter slit to the movement direction differs 90° between both movements, but the effect is negligible. Tomograms using a vortex beam $Q = 0$ as input beam produce identical results.

If we now select singly charged ($Q = 1$ and $Q = -1$) vortex beams (Fig. 3.6), the single bright spot splits into two and a zero-intensity singularity is visible. We can also notice that $Q = 1$ and $Q = -1$ are not identical (while their beam intensity profiles are), but produce mirrored tomograms [8] about the vertical axis. As we increase the vortex charge to $Q = \pm 3$ (Fig. 3.7), we note an increase in the split between the two bright areas and in their size.

The results are drastically different if a tomogram of a vortex beam is calculated by moving the slit vertically over a path located outside the beam's center. In Fig. 3.8, we find that the tomogram for a $Q = \pm 1$ vortex beam does not show the zero-intensity singularity as the traveling path is displaced from the beam's center ($d_0 = 7$ μm) when the waist parameter of the vortex is $w_0 = 7$ μm. Instead, a single ovoid shaped bright spot is seen. Still, the sign of the charge of the input vortex beams can be easily recovered.

Keeping the same displacement of the input beam's traveling path ($d_0 = 7$ μm) and increasing the charge to $Q = \pm 3$ (Fig. 3.9), we have tomograms with two bright spots slightly separated, that are each other's mirror, this time about the horizontal axis.

Figs. 3.10 and 3.11 show two vertical scans of $Q = \pm 1$ and $Q = \pm 3$ vortex beams, respectively, traveling through the beam's center ($d_0 = 0$). Compared with Fig. 3.6 and Fig. 3.7, these aren't slanted because the slit only travels through two constant "phases". These are features that will allow us to characterize a possible unknown incoming vortex beam.

Finally, because the experiments suggest that this may be happening, (Figs. 3.12 to 3.14) were calculated considering that some remaining direct light can travel through the SP receiver slit and therefore, interfere with scattered SPs. Although once we suspect that we have interference in our measurements, we know that the phase can no longer be recovered, it may be still possible to measure the sign of the charge of the input vortex beam, as shown in these tomograms.

In Figs. 3.17(a) and 3.17(b) we highlight the position and the intensity value of the maximum in each slice of the tomogram shown in Fig. 3.9(a). We also include in Fig. 3.17(c) the $Q = 3$ vortex beam phase profile as calculated from Eq. 3.1 from which we take the field amplitudes and the phase derivative taken over the path of the emitter slit movement (Fig. 3.17(d)). By comparing this two images, we find a good agreement, despite artifacts due to the finite resolution in the simulations and the size of the emitter slit, between the position and amplitude of the maximum value in each slice of the tomograms and the derivative of the field phase and the field amplitude.

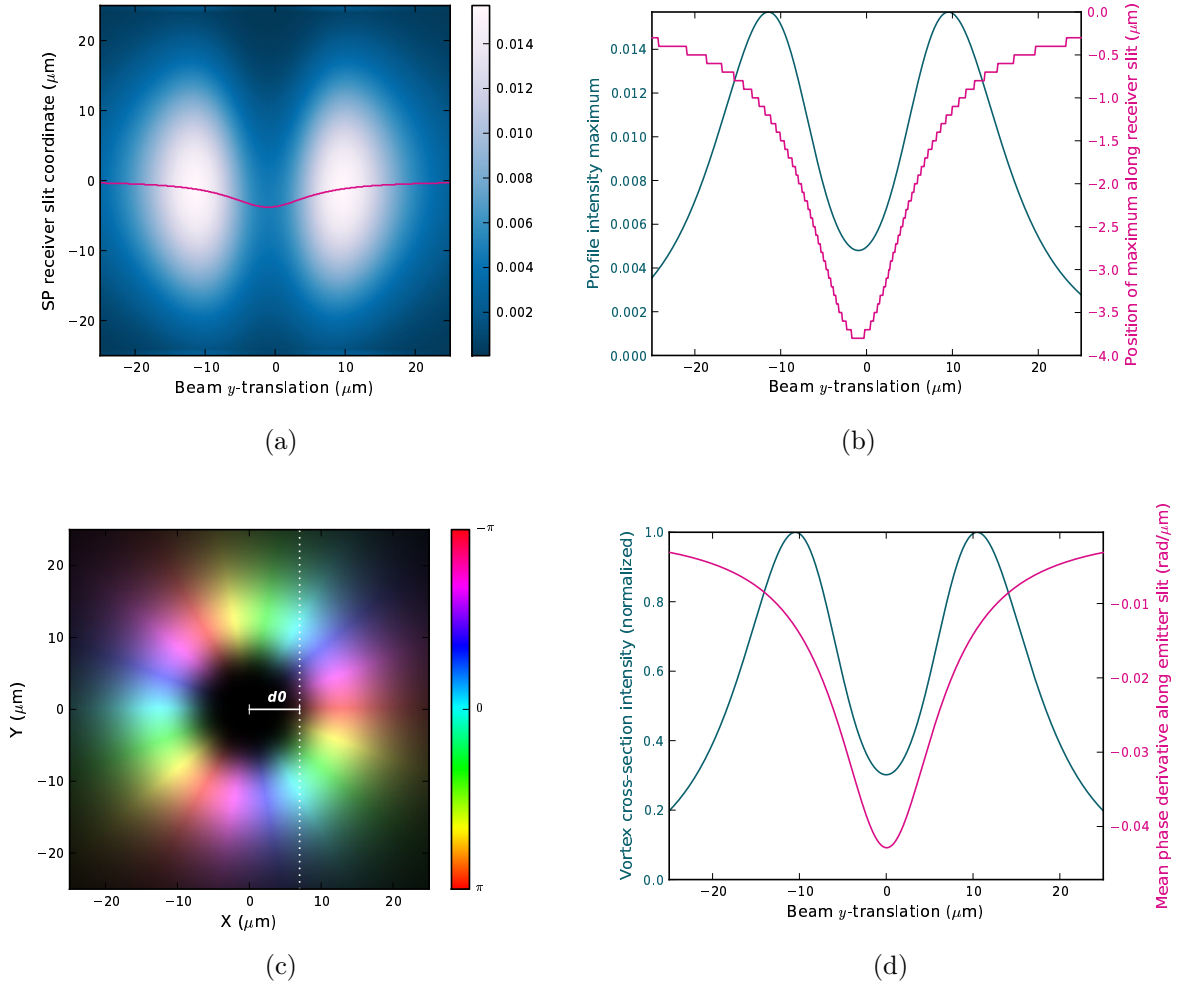

Figure 3.17: Distribution of (a) the position of the maximum and (b) its intensity in each slice of tomogram for a vortex beam $Q = 3$ in vertical movement (Fig. 3.9(a)). In (d) we show the calculated phase derivative and intensity over the path of the emitter slit movement ($d_0 = 7\mu$m) as highlighted in (c) the phase profile of the same input vortex beam.

By integrating 3.17(b) we can obtain the phase of the input beam shown in Fig. 3.18(a). For comparison, the phase directly calculated from the input vortex beam is shown in Fig. 3.18(b).

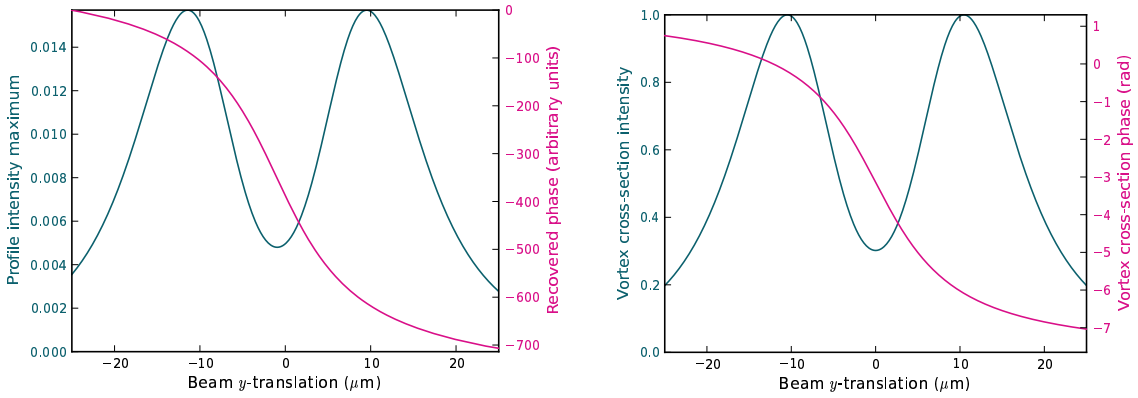

(a) (b)

Figure 3.18: By integrating 3.17(b) we can recover the phase as shown in (a). The phase directly calculated from the input vortex beam is shown in (b).

If we compare this result with that in Fig. 3.19 we can see that for opposite charge Q the orientation of the maximum position line tells us the sign of the charge.

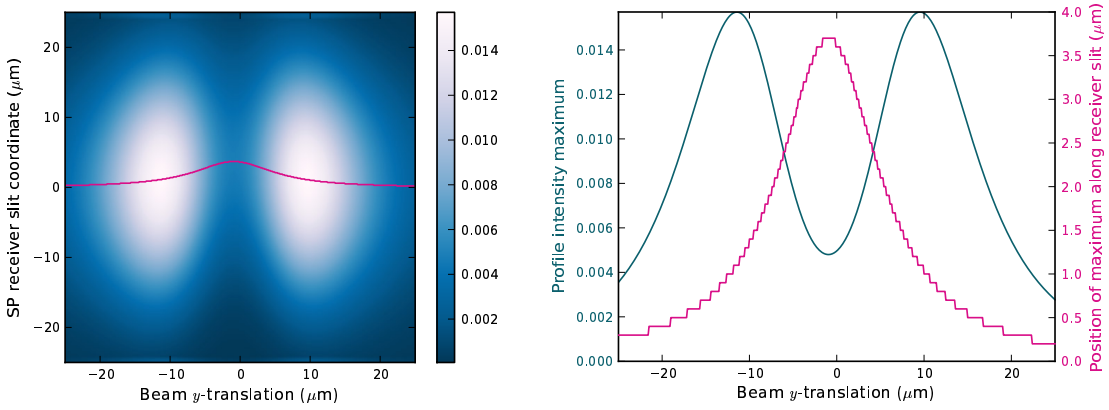

(a) (b)

Figure 3.19: Distribution of (a) the position of the maximum and (b) its intensity in each slice of tomogram for a vortex beam $Q = -3$ in vertical movement (Fig. 3.9(b)).

If we incorporate the interference of incoming remaining light that may reach the receiver slit in Fig. 3.17, the maximum position line changes completely and no longer gives us information about the original incident beam as shown in Fig. 3.20 as we would expect. This is a main reason why it is so important to isolate the receiver slit from any interference.

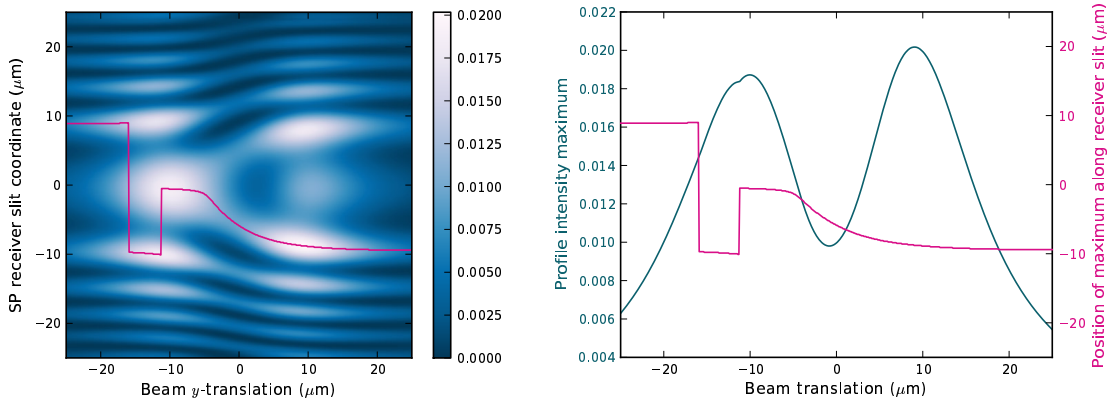

(a) (b)

Figure 3.20: Distribution of (a) the position of the maximum and (b) its intensity in each slice of tomogram for a vortex beam $Q = 3$ in vertical movement with remaining light in receiver slit causing interference.

Chapter 4

Experiment

The original experiment design included a sample with a collection of slit-groove pairs (Fig. 4.1(a)) where the depth of the grooves remained constant and the only variables were the length of the slits and the distance between the slits in the pair. Unfortunately, in practice, the grooves didn't convert the light back into free space. As an alternative, we tried to use the only structure in the sample were we could observe re-emitted SPs (Fig. 4.1(b)). This structure is the slit-slit pair that we have described through the rest of this work. Because we already know, as explained in section 3.2, that the interference of any remaining light with the re-emitted SPs in the receiver slit would hinder the capacity of this method to extract the desired phase information, the following experimental set-ups were constructed with the additional requirement of preventing any remaining light from the vortex beam from reaching the receiver slit.

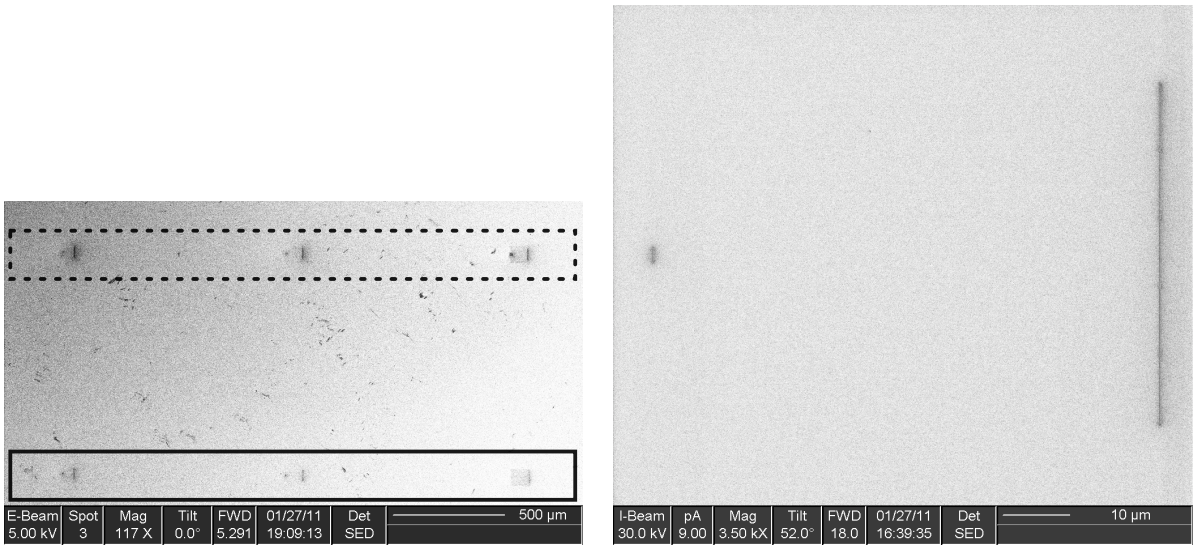

(a) (b)

Figure 4.1: Scanning electron microscope (SEM) pictures of (a) a wide field of the sample and (b) a magnification of the slit-slit pair that we used in the experiment. In the first picture, we can see a set of 3 slit-slit pairs (dotted line) and a set of 3 slit-groove pairs (solid line) that didn't work. The slit-slit pair in the second picture, is broadly described in Chapter 3.

4.1 Set-ups

This section describes the experimental set-up, which is shown in Fig. 4.2. One fiber-coupled diode laser emits a Gaussian beam ($\lambda = 830$ nm) that goes through a polarizer, a half-wave plate and finally to a dislocation holographic grating with broken grooves forming so called "fork" structures (more below). The linearly polarized beam is rotated using the half-wave plate such that it is perpendicular to the long dimension of the slits (TM polarization). The holographic grating produces many diffracted beams, each containing a vortex beam with different Q depending on the diffraction order. After selecting only one of the output vortex beams, we focused this beam onto the gold film through a scan lens using a motorized scanning mirror. This mirror can rotate about two axes and together with the scan lens, it is specialized in translating the vortex beam over the SP emitter slit during the measurements while maintaining the focus. Finally, the generated beam in the SPs receiver slit will be imaged onto a CCD camera by an objective.

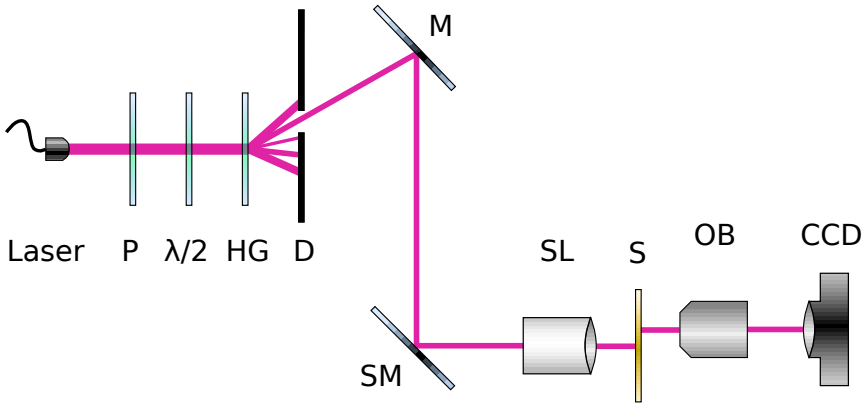

Figure 4.2: First experimental set-up. P is a polarizer, $\lambda/2$, a half wave plate, HG, an holographic grating, D, a diaphragm, M, a fixed mirror, SM, a motorized scanning mirror, SL, a scan lens, S, the sample, OB, an objective and CCD, a CCD camera.

A scan lens is a telecentric objective named liked that because it is usually used to scan a laser beam across the back aperture of the objective lens in order to form the image of a given sample. Each position that the laser is scanned over corresponds to one point in the image formed. This approach results in a focal spot on the sample that is not, in general, coincident with the optical axis of the scan lens. In traditional lenses, this would result in the introduction of severe aberrations that would significantly degrade quality of the resulting image. However, the scan lens used in this experiment creates a uniform spot size and optical path length for the laser for every scan position, which allows a uniform, high-quality, image of the sample to be formed. A telecentric scan lens also maximizes the coupling of the light scattered or emitted from the sample (the signal) into the detection system. In addition, the spot size in the image plane is nearly constant over the entire field of view so that resolution of the image is constant.

A fork holographic grating is a diffractive element containing a fork dislocation [17]. This grating, when illuminated with a Gaussian beam, for example, from a single-mode fiber, produces the helical mode in the first diffraction orders (Fig. 4.3). Physically, a diffracted beam is formed as a result of interference between the "regular" diffracted wave originating from the

grating and the divergent "singular" wave that originates from the bifurcation point in the hologram center. The singular wave amplitude possesses much lower magnitude rapidly decreasing with growing topological charge of the resulting beams. The grating used in this experiment produces vortex beams with only odd values of Q for this wavelength.

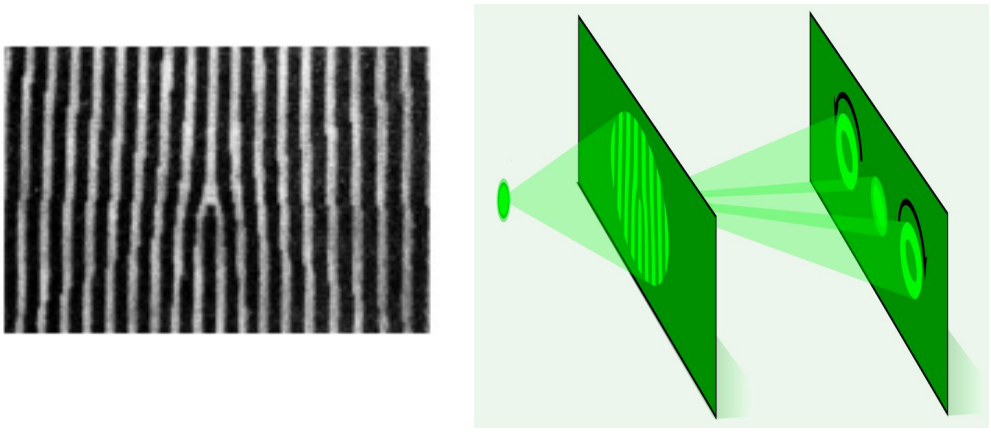

(a) (b)

Figure 4.3: (a) Image of a fork holographic grating (reproduced from [17]) that produces beams with a first-order dislocation. (b) A fork holographic grating transforms a beam from a single-mode fiber into a series of doughnut shaped beams (Giorgio Volpe 2011 © Optics & Photonics Focus).

Eventually, due to practical difficulties at obtaining the desired results, two extra set-ups, modified versions of the original one, were constructed. These difficulties were mainly caused by some remaining light coming from the vortex beam, that was traveling directly through the receiver slit, interfering with the SPs. Fig. 4.4 shows the second set-up, where a razor blade is placed at the working distance of the scan lens in order to block all the remaining light that could reach the receiver slit. Also, a single lens is introduced at twice the focal length, in between the razor and the sample to image the reshaped beam on to the sample.

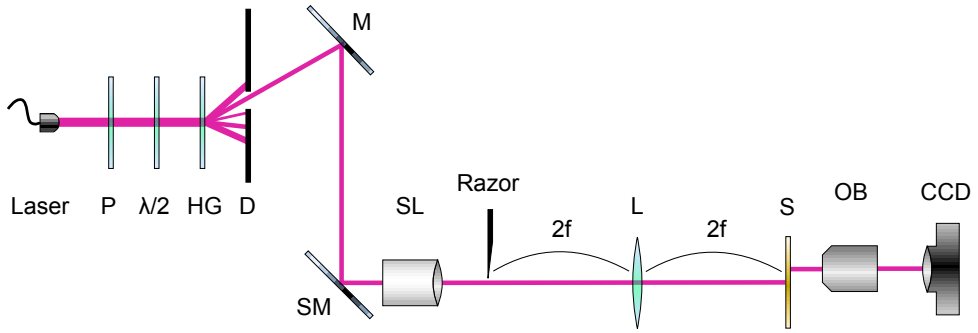

Figure 4.4: Second experimental set-up based on the first one. A single lens and a razor blade are introduced in order to block the excess light from reaching the sample.

The third set-up (Fig. 4.5), simply introduces a screen next to the sample at a distance less than 1 mm, just in front of the receiver slit with the same purpose. The improvements in

the second and third set-ups were successfully applied by at least one member of our research group in his own experiments (unpublished).

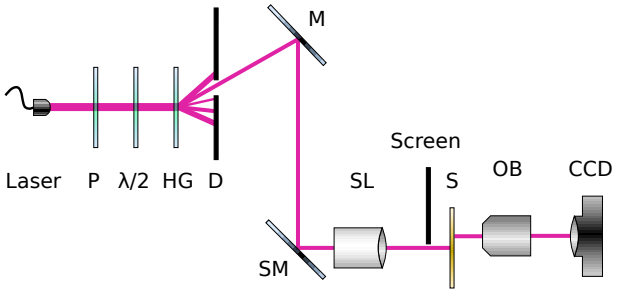

Figure 4.5: Third experimental set-up based on the first one. A screen is introduced in order to block the excess light from reaching the sample.

4.2 Results

In this section, we present the experimental results we obtained in the second and third set-ups at reproducing the simulations in the lab. The approximate value of the waist parameter of the host Gaussian beam varies in every case. We start with the tomograms for a Gaussian beam in horizontal (Fig. 4.6(a)) and vertical movements (Fig. 4.6(b)). We can see that experimental and expected results shown in Fig. 3.5 differ in the size and shape of the bright spot although our experimental results are comparable in size and shape between each other as expected. However, when we compare these results to the ones in Fig. 3.12 where we incorporate interference with directly transmitted light through the receiver slit, we find a clear similarity in structure.

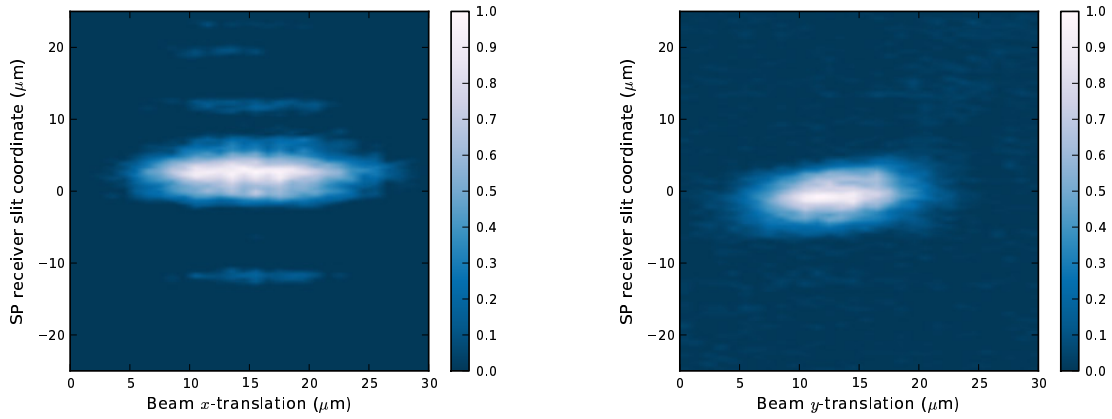

(a) (b)

Figure 4.6: Experimental tomogram of a Gaussian beam with a waist parameter, $w_0 \approx 40$ μm, in (a) horizontal and (b) vertical movements obtained using the third set-up.

In Fig. 4.7 we show two experimental attempts of tomograms of a vortex beam $Q = 1$ with vertical movement. Comparing them with the corresponding simulations without interference (Fig. 3.8), we find that both are quite different in structure. However, looking at the simulations with interference (Fig. 3.13) we do find some similarities. Note, for example, how the edges and outer fringes of the central feature are comparable.

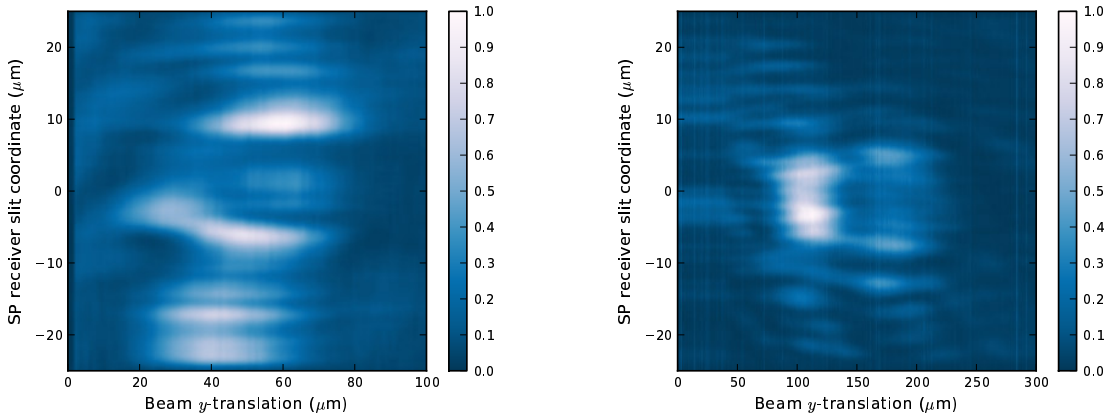

(a) (b)

Figure 4.7: Experimental tomograms of a $Q = 1$ vortex beam in vertical movement obtained using the third set-up with $d_0 \approx 20$ μm. The waist parameter of the host Gaussian beam is $w_0 \approx 30$ μm.

Fig.4.8 is an example of tomograms obtained for a vortex beam $Q = -3$ in vertical movement in the second set-up. As can be seen, no clear similarity was found between these results and the simulation shown in Fig. 3.9(b) for a vortex beam with this charge. The simulation shown in Fig. 3.14(b) however, clearly resembles the arrow-like shape as found in the experiment.

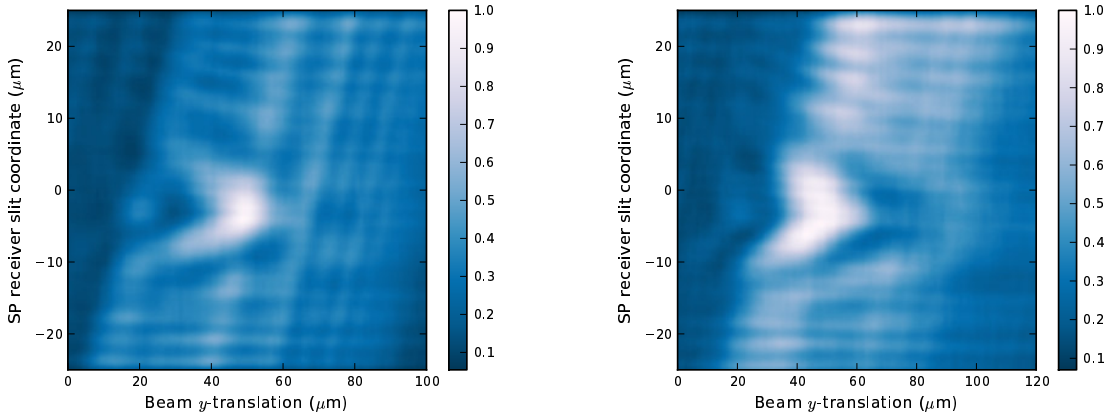

(a) (b)

Figure 4.8: Experimental tomograms of a $Q = 3$ vortex beam in vertical movement obtained using the second set-up with $d_0 \approx 10$ μm. The waist parameter of the host Gaussian beam is $w_0 \approx 7$ μm.

It is interesting to note that even though the interference in all our results do not allow us to recognize the phase of the incoming beam, it does tell us what the sign of its charge is.

Chapter 5

Conclusions

The aim of this project was to find an alternative method for the phase retrieval problem using SP properties. By simulating the generation of SPs by scattering an incoming vortex beam on a narrow emitter slit milled in a gold film and the re-conversion to light of the diffracted SP wave by a receiver and then, by translating the sample along the positive x-axis and positive y-axis, we constructed a tomographic pattern of the plasmonic diffraction where each vertical slice of the tomogram corresponded to one local sample of the incident vortex beam after propagation from emitter to receiver. These simulated tomograms gave us both the phase and intensity of the incoming vortex beam as intended, thus, solving the phase retrieval problem at least on paper.

The first attempt to perform this experiment in the lab included the use of a gold film with different slit-groove pairs. These structures weren't able to convert the SPs back to light. Trying to find an alternative approach for this problem, we decided to use a slit-slit structure milled in the same sample. We tried with different experimental set-ups to avoid incoming light reaching the receiver slit that could interfere with the re-emitted light coming from the SPs, since we demonstrated that this interference is a major obstacle in the retrieval of phase information. Unfortunately, none of these attempts successfully avoid such interference.

The main possible explanation for the failure of the original slit-groove structures, as discussed in section 2.2.4, is related to the depth of the grooves. Because of our results using the slit-slit system show that the original approach of using emitter grooves instead of emitter slits is still a possible solution, since it avoids the interference problem, we strongly suggest that the next step in this project will be the construction of a sample with the same features as the one that we used, but with a set of slit-groove structures where the only variable will be the depth of the groove.

Some of the designs already constructed in the gold film used in this work included variations of the slit-groove pairs such as the distance between the indentations and their relative size. Moreover, by changing the emitter slit into an L-shaped slit and by allowing two receiver grooves to radiate at either end, we would expect to measure the two polarization components of the local input field, creating a polarization sensitive structure (2-dimensional scanning of the input field). Along with the intensity and the phase information, knowing the polarization would result in a complete characterization of an unknown incoming beam. These structures should not be ignored in future projects.

Acknowledgments

I would like to thank Eric Eliel for offering me the opportunity to participate in this research project and for his sharp advices. Also, I would like to thank Sumant Oemrawsingh for helping me on my very first steps on Python, Wolfgang Löffler for helping me finding my way on the drawers of the lab, Martin van Exter for his suggestions on the experimental settings, Prof. Nienhuis for boosting conversations and Louwrens van Dellen for his personal Labview for dummies manual.

I am specially grateful with Philip Chimento for his support in every single step of this project. His patience, his ability to make clear and simple statements and his joyful personality made the realization of this work possible and worthwhile.

Finally, I would like to thank CONACYT for the financial support that made possible this whole adventure and my parents for their unconditional support.

Bibliography

[1] D. C. Redding, F. Shi, S. A. Basinger, D. Cohen, J. I. Green, A. E. Lowman and C. M. Ohara, "Wavefront Sensing and Control for Large Space Optics", Aerospace Conferences IEEE 4, 1729-1744 (2003).

[2] H. A. Hauptman, "The phase problem of X-ray crystallography", Rep. Prog. Phys. 54, 1427-1454 (1991).

[3] R. W. Gerchberg and W. O. Saxton, "A practical algorithm for the determination of phase from image and diffraction plane pictures", Optik 35, 237-246 (1972).

[4] J. Fienup, "Reconstruction of an object from the modulus of its Fourier transform", Opt. Lett. 3, 27-29 (1978).

[5] H. H. Bauschke, P. L. Combettes and D. R. Luke, "Phase retrieval, error reduction algorithm and Fienup variants: a view from convex optimization", J. Opt. Soc. Am. A 19, 1334-1345 (2002).

[6] H. W. Babcock, "The possibility of compensating astronomical seeing", Pub. Astr. Soc. Pac. 65, 229-236 (1953).

[7] H. I. Campbell and A. H. Greenaway, "Wavefront Sensing: From Historical Roots to the State-of-the-Art", EAS Publ. Series 22, 165-185 (2006).

[8] P. F. Chimento, G. W. 't Hooft and E. R. Eliel, "Plasmonic tomography of optical vortices", Opt. Lett. 35, 3775-3777 (2010).

[9] H. Raether, "Surface plasmons on smooth and rough surfaces and on gratings", Springer Tracts in Modern Physics 111, Springer-Verlag, Berlin (1988).

[10] A. Archambault, T. V. Teperik, F. Marquier and J. J. Greffet, "Surface plasmon Fourier optics", Phys. Rev. B 79, 195414(1-8) (2009).

[11] T. V. Teperik, A. Archambault, F. Marquier and J. J. Greffet, "Huygens-Fresnel principle for surface plasmons", Opt. Express 17, 17483-17490 (2009).

[12] H. F. Schouten, N. Kuzmin, G. Dubois, T. D. Visser, G. Gbur, P. F. A. Alkemade, H. Blok, G. W. 't Hooft, D. Lenstra and E. R. Eliel, "Plasmon-Assisted Two-Slit Transmission: Young's Experiment Revisited", Phys. Rev. Lett. 94, 53901(1-4) (2005).

[13] J. A. Sanchez-Gil and A. A. Maradudin, "Near-field and far-field scattering of surface plasmon polaritons by one-dimensional surface defects", Physical Rev. B 60, 8359-8367 (1999).

[14] A. Ya. Bekshaev and A. I. Karamoch, "Spatial characteristics of vortex light beams produced by diffraction gratings with embedded phase singularity", Opt. Communications 281, 1366-1374 (2008).

[15] E. D. Palik, "Handbook of Optical Constants of Solids", Vol. 2, Academic Press, Boston (1985).

[16] P. F. Chimento, N. V. Kuzmin, J. Bosman, P. F. A. Alkemade, G. W. 't Hooft and E. R. Eliel, "A subwavelength slit as a quarter-wave retarder", Opt. Express 19, 24219-24227 (2011).

[17] V. Y. Bazhenov, M. V. Vasnetsov and M. S. Soskin, "Laser beams with screw dislocations in their wavefronts", JETP Lett. 52, 429-431 (1991).